PROCEEDINGS, 49th Workshop on Geothermal Reservoir Engineering
Stanford University, Stanford, California, February 12-14, 2024
SGP-TR-227

Modeling of Diagnostic Fracture Injection Tests for In Situ Stress Characterization of the Utah FORGE Reservoir

Fan Fei[a], Chaoyi Wang[a], Matteo Cusini[a], Luke P. Frash[b], Kayla A. Kroll[a]

[a]Atmospheric, Earth, and Energy Division, Lawrence Livermore National Laboratory, USA

[b]Earth and Environmental Sciences Division, Los Alamos National Laboratory, USA

E-mail address: fei2@llnl.gov

Keywords: DFIT, hydraulic fracturing modeling, in situ stress estimation, Utah FORGE

ABSTRACT

Diagnostic fracture injection tests (DFITs) are used to estimate the minimum horizontal stress in a target reservoir through analysis of the pressure response during the controlled injection process. The in situ stress conditions inferred from DFIT tests are crucial for designing and optimizing the stimulation and circulation processes in enhanced geothermal systems (EGS). In this work, we employ a coupled finite-element/finite-volume numerical simulator to model DFITs in EGS settings. To better model the characteristics of fracture closure for more accurate predictions of the pressure response during the shut-in stage, we integrate stress-dependent aperture models (e.g., the Barton–Bandis model (Barton, et al., 1985) and an exponential model (Li, et al., 2021) fit to experimental data) into an established hydraulic fracturing solver. Then, we apply the solver to history match the pressure data observed in the injection and shut-in activities in Zone 2 of Well 58-32 at the Utah-FORGE site. The fracture properties adopted in the model are derived from tri-axial direct-shear experiments on granite samples collected from the Utah-FORGE site. In the simulation, the thermal effects on DFIT response are investigated by comparing predictions under isothermal and non-isothermal conditions. The findings from this numerical study provide insights into identifying in situ stress conditions and the role of thermal processes in the Utah-FORGE reservoir.

1. INTRODUCTION

In 2018, the U.S. Department of Energy has initiated the Utah FORGE (Frontier Observatory for Research in Geothermal Energy) project, aiming to advance EGS technologies through innovative research and field testing. In 2017 and 2019, a series of injection tests were performed in a pilot well 58-32 at the Utah-FORGE site to estimate the in situ stress. These injection activities were conducted in three separate zones, isolated with packers and bridge plugs during tests. Zone 1 is an open-hole section at the toe of the well, while Zones 2 and 3 are both 3-m long cased and perforated sections above Zone 1. A detailed description of the site geology, Well 58-32, and all injection cycles can be found in Xing et al. (2020). In this analysis, we model hydraulic fracture growth and closure to capture the characteristics of the *Cycle 4* DFIT in Zone 2, in order to understand the in situ stress conditions at the site.

DFITs are a common type of the injection test performed in subsurface energy systems. These tests provide important information such as fracture closure pressure and instantaneous shut-in pressure (ISIP), from which in situ stress conditions can be inferred. During typical DFITs, the well-head pressure is measured across two stages: (1) a controlled injection stage to create a small hydraulic fracture, and (2) a shut-in stage where injection is stopped and the hydraulic fracture gradually closes as fluid inside leaks into surrounding rock matrix. The pressure data are then used in various analyses including *G*-function tests (Economides & Nolte, 1989; McClure, et al., 2016) to recover the stress conditions.

In this paper, we present a numerical study of the DFITs conducted at the Utah FORGE site using a high-fidelity geomechanical simulator, i.e., the hydraulic fracturing module of the GEOS simulation framework. The hydraulic fracturing solver employs a fully-coupled finite element/finite volume approach to solve the coupled solid mechanics and fluid flow equations, with propagating fractures located at the interface between grid cells (Settgast, et al., 2017). Also, GEOS has integrated appropriate hydraulic aperture models into the hydraulic fracturing solver to accurately capture the nonlinear fracture closure behavior during the shut-in stage. Here, we employ this numerical method to model a DFIT conducted at the Utah FORGE site by calibrating in situ stresses and material parameters based on their reference values from relevant literature and experimental measurements.

The simulation results indicate that the adopted hydraulic fracturing model coupled with the selected hydraulic aperture model can well reproduce the DFIT data from Utah FORGE as long as appropriate parameters are used. Notably, the calibrated minimum horizontal stress and all material parameters are consistent with those found in the literature and through relevant experiments. Further, a non-isothermal DFIT simulation demonstrates minimal thermal effects on the pressure response, due to the limited injection volume and lack of pre-cooling before the DFIT.

2. FORMULATION

This section summarizes the formulations for modeling the DFIT in GEOS including governing equations and fracture propagation criterion. Subsequently, the non-linear hydraulic aperture models of interest are presented and incorporated into the model to better capture the fracture closure response.

2.1 Governing Equations

Let us consider a porous domain Ω with its exterior boundary denoted by $\partial\Omega$. The exterior boundary is decomposed into two non-overlapping regions subject to Dirichlet and Neumann boundary conditions, respectively. These are identified with $\partial_u\Omega$ and $\partial_t\Omega$ for the solid mechanics equations, $\partial_p\Omega$ and $\partial_q\Omega$ for the fluid flow ones, and they satisfy $\partial_u\Omega \cup \partial_t\Omega = \partial\Omega$, $\partial_u\Omega \cap \partial_t\Omega = \emptyset$, and $\partial_p\Omega \cup \partial_q\Omega = \partial\Omega$, $\partial_p\Omega \cap \partial_q\Omega = \emptyset$. The domain also contains a set of fluid-driven fractures denoted by Γ.

Neglecting body forces, the equations that describe quasi-static deformation of a solid containing a fracture are

$$\nabla \cdot \boldsymbol{\sigma} = \mathbf{0} \quad \text{in } \Omega, \tag{1}$$

$$\boldsymbol{\sigma} \cdot \boldsymbol{n}_{\partial\Omega} = \hat{\boldsymbol{t}} \quad \text{on } \partial_t\Omega, \tag{2}$$

$$\boldsymbol{u} = \hat{\boldsymbol{u}} \quad \text{on } \partial_u\Omega, \tag{3}$$

$$\boldsymbol{\sigma} \cdot \boldsymbol{n}_{\Gamma+} = -\boldsymbol{\sigma} \cdot \boldsymbol{n}_{\Gamma-} = -p_f \boldsymbol{n}_{\Gamma+} + \boldsymbol{t}_\Gamma \quad \text{on } \Gamma. \tag{4}$$

Here, $\boldsymbol{\sigma}$ is the stress tensor, which can be calculated below if assuming an isotropic linear elastic material,

$$\boldsymbol{\sigma} = \left[\frac{E\nu}{(1+\nu)(1-2\nu)} \mathbf{1} \otimes \mathbf{1} + \frac{E}{1+\nu} \boldsymbol{I}\right] : \boldsymbol{\varepsilon}, \tag{5}$$

where $\boldsymbol{\varepsilon}$ is the strain tensor, E and ν are the elastic modulus and Poisson's ratio, respectively, $\mathbf{1}$ and $\boldsymbol{I}$ are second-order and fourth-order identity tensors, respectively. In Eqs. (2) and (3), $\hat{\boldsymbol{t}}$ and $\hat{\boldsymbol{u}}$ are the prescribed traction and displacement on the exterior boundary, respectively, and $\boldsymbol{n}_{\partial\Omega}$ is the unit vector normal to $\partial_t\Omega$. Equation (4) describes a stress continuity constraint across Γ, where $\boldsymbol{n}_\Gamma$ is the outward normal vector of Γ, p_f represent the fluid pressure inside the fracture, and $\boldsymbol{t}_\Gamma$ is the contact force. For simplicity, we ignore the shear force on the fracture and only consider the normal component of $\boldsymbol{t}_\Gamma$, thus $\boldsymbol{t}_\Gamma$ can be expressed by

$$\boldsymbol{t}_\Gamma = -\sigma_\mathrm{N} \boldsymbol{n}_\Gamma. \tag{6}$$

Here, σ_N is the magnitude of contact normal stress. In this work, a penalty method is employed to weakly enforce contact constraints, and σ_N is given by

$$\sigma_\mathrm{N} = \begin{cases} 0 & \text{if } \omega_m > 0, \\ -K_\mathrm{N}\omega_m & \text{if } \omega_m \leq 0, \end{cases} \tag{7}$$

where K_N is the penalty stiffness[1], and $\omega_m := (\boldsymbol{u}_{\Gamma+} - \boldsymbol{u}_{\Gamma-}) \cdot \boldsymbol{n}_\Gamma$ refers to the mechanical aperture of the fracture.

The momentum balance equation is coupled to the equations describing mass balance both in the rock matrix and in the fracture (denoted by subscripts m and f, respectively). For the rock matrix, the single-phase mass balance equation is given by

$$\frac{\partial}{\partial t}(\rho_f \phi) + \nabla \cdot (\rho_f \boldsymbol{v}_m) + q_{fm} = q_{ms} \quad \text{in } \Omega \setminus \Gamma, \tag{8}$$

and is subject to the following boundary conditions,

$$\boldsymbol{v}_m \cdot \boldsymbol{n}_{\partial\Omega} = \hat{v}_m \quad \text{on } \partial_q\Omega, \tag{9}$$

$$p_m = \hat{p}_m \quad \text{on } \partial_p\Omega. \tag{10}$$

Here, ρ is the fluid density, ϕ is the matrix porosity, $\boldsymbol{q}_m$ is the flux rate in the matrix, q_{ms} is the source/sink term in the matrix, $\hat{v}_m$ and $\hat{p}_m$ are prescribed flux and matrix pressure on the corresponding portion of the boundary. q_{fm} is a term indicating the mass exchange between the rock matrix and the fracture. According to Darcy's law, the fluid velocity in rock matrix $\boldsymbol{v}_m$ is

$$\boldsymbol{v}_m = -\frac{k}{\mu} \nabla p_m, \tag{11}$$

where k is the matrix permeability and μ is the fluid viscosity. Furthermore, both the fluid and the porous matrix are compressible and the following constitutive relationships are considered for the fluid density and the rock porosity:

$$\rho = \rho_0[1 + C(p_m - p_0)], \tag{12}$$

$$\phi = \phi_0[1 + C_\phi(p_m - p_0)]. \tag{13}$$

---

[1] $K_\mathrm{N} = 10^3$ GPa is used in this work.

Here, ρ_0 is the reference fluid density, C is the fluid compressibility, C_ϕ is the pore compressibility, p_0 is the reference pressure, ϕ_0 is the reference matrix porosity.

The mass balance equation inside the fracture is given by

$$\frac{\partial}{\partial t}(\rho \omega_h) + \nabla \cdot (\rho\, \omega_h \boldsymbol{v}_f) + q_{mf} = q_{fs} \quad \text{in } \Gamma, \tag{14}$$

where ω_h is the hydraulic aperture of the fracture, $\boldsymbol{v}_f$ denotes the fluid velocity inside the fracture, q_{mf} is the mass exchange between the fracture and the porous matrix, and q_{fs} is the source/sink term in the fracture. According to the lubrication theory (Batchelor, 1967), the fluid velocity in the fracture, $\boldsymbol{v}_{f,}$ is

$$\boldsymbol{v}_f = -\frac{\omega_h^2}{12\mu} \nabla p_f. \tag{15}$$

The hydraulic aperture (ω_h) is a function of the state of stress and, in this work, is updated according to the constitutive relationships described in Section 2.3.

To model fracture propagation induced by fluid injection, we use linear elastic fracture mechanics (LEFM) combined with an advanced virtual crack closure technique (VCCT). This method calculates the stress intensity factor, K_I, at the crack tip. Fracture extension occurs when K_I reaches or exceeds the rock's fracture toughness K_{Ic}, forming new cracks by separating nodes between adjacent elements. While this paper does not detail the enhanced VCCT, further information is available in Wu et al. (2021).

2.2 Hydraulic Aperture Models

Existing analytical solutions and most numerical models of hydraulic fracturing assume a perfectly smooth fracture surface, where the hydraulic aperture is identical to the mechanical aperture. However, ample experimental evidence indicates that rock fractures have rough surfaces, which create a complex nonlinear relationship between the contact normal stress and the fracture hydromechanical properties (e.g., hydraulic aperture). The fracture closure response during the shut-in stage of a DFIT is closely related to the relationship between the contact normal stress and the hydraulic aperture.

In this work, we consider two distinct constitutive relations between the hydraulic aperture ω_h and contact normal stress σ_N. The first relation is derived from the Barton–Bandis model (Barton, et al., 1985), reformulated by Willis-Richards et al. (1996) as

$$\omega_h = \frac{\omega_0}{1+9\sigma_\mathrm{N}/\sigma_\mathrm{ref}}. \tag{16}$$

Here, ω_0 is the hydraulic aperture at zero contact stress (i.e., $\sigma_\mathrm{N} = 0$), and σ_ref is the reference contact stress at $\omega_h = 0.1\omega_0$. The second relation is an exponential formulation originating from Li et al. (2021), given by

$$\omega_h = \omega_0 \exp(-\alpha\sigma_\mathrm{N}), \tag{17}$$

where α is a model parameter characterizing the fracture compressibility.

For a meaningful comparison between the two models, the equivalent fracture compressibility term α can be computed using σ_ref to ensure that both models intersect at the reference aperture (i.e., $\omega_h = 0.1\omega_0$). The equivalent fracture compressibility is given by

$$\alpha = \frac{\ln 10}{\sigma_\mathrm{ref}}. \tag{18}$$

It is also useful to compare the fracture stiffness, defined as $-\mathrm{d}\sigma_\mathrm{N}/\mathrm{d}\omega_h$, between the two models. For the Barton–Bandis model (16), the fracture stiffness is

$$K_{f,\text{Barton–Bandis}} = -\frac{\mathrm{d}\sigma_\mathrm{N}}{\mathrm{d}\omega_h} = \frac{\sigma_\mathrm{ref}}{9}\frac{(1+9\sigma_\mathrm{N}/\sigma_\mathrm{ref})^2}{\omega_0}, \tag{19}$$

while for the exponential model (17), is

$$K_{f,\text{exponential}} = -\frac{\mathrm{d}\sigma_\mathrm{N}}{\mathrm{d}\omega_h} = \frac{\sigma_\mathrm{ref} 10^{\sigma_\mathrm{N}/\sigma_\mathrm{ref}}}{\omega_0 \ln 10}. \tag{20}$$

Figure 1 presents a comparative plot of two relationships with $\omega_0 = 15$ mm, $\sigma_\mathrm{ref} = 65$ MPa, and an equivalent fracture compressibility $\alpha = 0.035$ MPa^{-1}. As can be seen, the two relations exhibit distinct shapes, due to the difference in their fracture stiffness. In Section 4.4, we compare the simulation results obtained from these two models and evaluate their applicability to Utah FORGE injection tests.

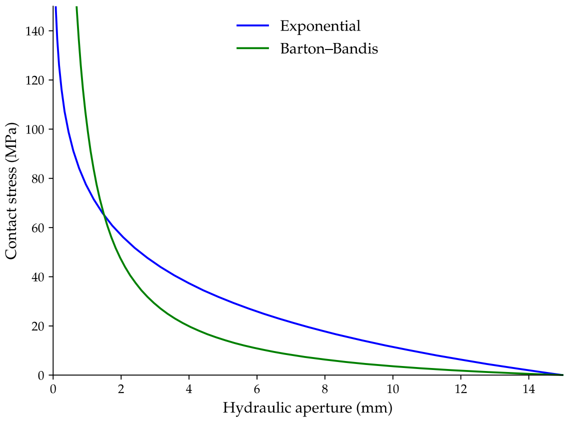

Figure 1: Comparison between two hydraulic aperture models with $\omega_0 = 15$ mm, $\sigma_{\mathrm{ref}} = 60$ MPa, and $\alpha = 0.035$ MPa^{-1}.

So far, we solely focus on the aperture when the fracture is closed (i.e., $\omega_m \leq 0$) while neglecting the open state (i.e., $\omega_m > 0$), which is prevalent during the injection stage and also the early phase of the shut-in stage before fracture closure begins. Clearly, neither Eq. (16) nor Eq. (17) is suitable to calculate ω_h when the fracture is open, as σ_{N} is zero according to Eq. (7). To account for the open aperture evolution, we assume the open fracture resembles two parallel plates with uniform residual aperture of ω_0. This assumption implies that both ω_h and ω_m change at the same rate while the fracture is open. Therefore, the complete form of ω_h is given by

$$\omega_h = \begin{cases} \omega_0 + \omega_m & \text{if } \omega_m > 0, \\ \text{Eq. (16) or (17)} & \text{if } \omega_m \leq 0. \end{cases} \tag{21}$$

3. NUMERICAL SOLUTION STRATEGY

3.1 Solution Procedure

To enhance numerical convergence and facilitate parameter calibration, the DFIT modeling workflow is divided into two phases, as illustrated in Figure 2. The first phase includes the simulation of fluid injection and fracture propagation until shut-in begins. Subsequently, in the second phase, the modeled hydraulic fracture geometry and pressure results are processed and imported to a separate model to simulate fluid leak-off and fracture closure during the shut-in period during which the hydraulic fracture no longer propagates. Material parameters, in situ stresses, and hydro-static pressure are kept consistent in both phases to ensure a coherent and accurate representation of the hydraulic fracture's behavior throughout the simulation process.

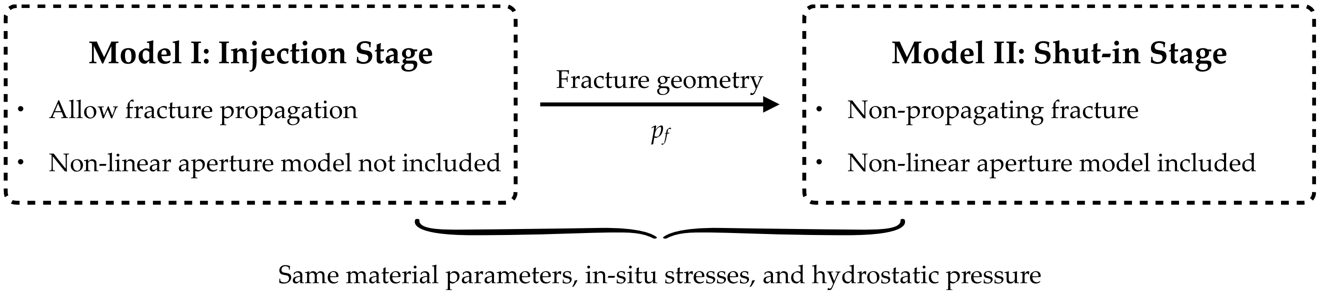

Figure 2: Workflow employed for DFIT modeling that separately solves injection and shut-in stages.

3.2 Numerical Discretization and Solution Algorithm

Equations (1), (8), and (14) are discretized in space with a low-order finite element discretization of the mechanical equations coupled to a finite volume discretization of the mass balance equations. An Euler backward method is employed for time discretization, so the nonlinear system of discrete equations is solved using a Newton-Raphson method at each time step. During the computation of Eq. (15), we utilize ω_h from the previous time step solution to improve convergence of the Newton-Raphson method. Upon convergence, the propagation criterion is evaluated to determine whether propagation has occurred. When the fracture propagates, the entire system is re-evaluated for the new fracture configuration until the fracture tip ceases to extend. This iterative process allows us to accurately resolve the evolving fracture geometry and associated physical properties until a stable configuration is reached.

4. MODELING OF A DFIT AT UTAH FORGE VERTICAL WELL 58-32

In this section, we employ the formulation and numerical method provided in the previous sections to simulate the injection test performed in the Utah FORGE reservoir, specifically *Cycle 4* within Zone 2 of Well 58-32. The injection rate and bottom hole pressure (BHP) recorded in the test are presented in Figure 3. Here, the BHP is obtained by adding the hydrostatic pressure to the casing pressure reported in GDR submission 1149.

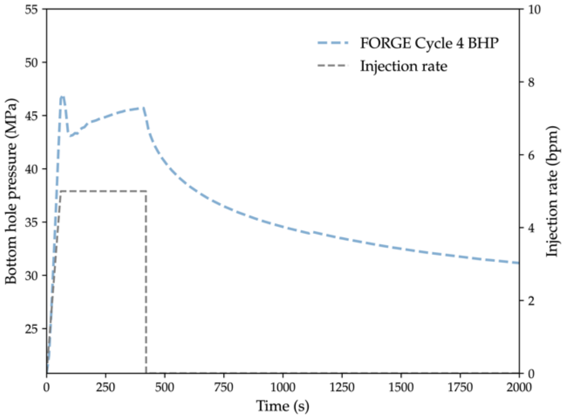

Figure 3: Field injection data and bottom hole pressure for Zone 2 Cycle 4 in Well 58-32.

4.1 Problem Geometry and Boundary Conditions

The model domain is a 200 m × 200 m × 200 m cubic domain as shown in Figure 4, subjected to in situ stresses and initial hydrostatic pressure. All boundaries of the domain are supported by rollers, and Table 1 and Table 2 list the initial conditions and the material parameters adopted in the simulation. The hydraulic fracture is assumed to be penny-shaped and propagates in the direction normal to the minimum horizontal stress σ_h. Interestingly, the observed BHP in Figure 3 steadily increases after the peak breakdown pressure, inferring that the height of the hydraulic fracture may be constrained within a layer due to high-stress barrier, which would lead to a Perkins-Kern-Nordgren (PKN) fracture geometry (Perkins & Kern, 1961; Nordgren, 1972). However, to the best of our knowledge, there is no evidence of such layering at Utah FORGE, thus, we assume a penny-shaped fracture geometry. The fluid injection is applied in the middle of the initial fracture at the injection rate shown in Figure 3 (grey curve).

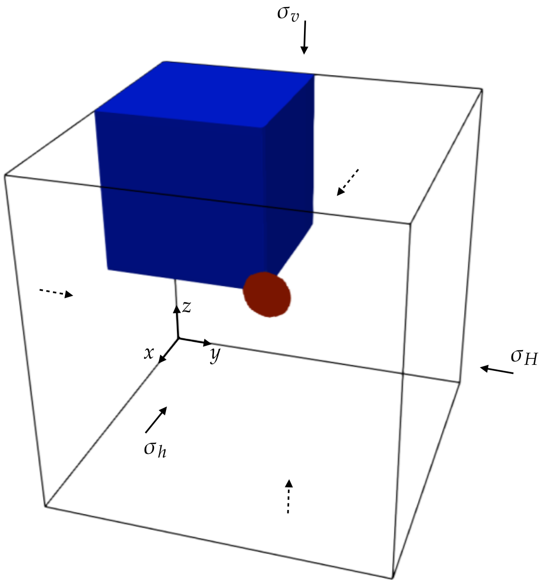

Figure 4: Schematic of the problem domain and boundary conditions.

4.2 Model Calibration

The matrix permeability, the minimum horizontal stress, the hydraulic aperture model and the related parameters (i.e., ω_0, σ_{ref}, and α) are calibrated to reproduce the field BHP curve (Figure 3). Hydrostatic pressure, in situ stress ratios (i.e., σ_H/σ_h, σ_v/σ_h), and other material parameters are consistent with those used in Xing et al. (2021).

Table 1: Initial conditions in the simulation

Minimum horizontal stress, σ_h	44.5 MPa
Maximum horizontal stress, σ_H	50.7 MPa
Vertical stress, σ_v	65.2 MPa
Hydrostatic pressure, p_0	20.8 MPa

Table 2: Rock and fluid properties in the simulation

Elastic modulus, E	50 GPa	Fluid viscosity, μ	1 cp
Poisson's ratio, ν	0.25	Fluid compressibility, C	5×10^{-4} MPa^{-1}
Fracture toughness, K_{Ic}	1.75 MPa·m$^{1/2}$	Initial aperture, ω_0	15 mm
Matrix permeability, k	8×10^{-16} m^2	Reference contact stress, σ_{ref}	65 MPa
Reference porosity, ϕ_0	0.01	Equivalent fracture compressibility, α	0.035 MPa^{-1}
Pore compressibility, C_ϕ	1.9×10^{-3} MPa^{-1}		

Simulation results obtained with the exponential model (17) and calibrated parameters are presented in Figure 5(a). The GEOS simulation results show a reasonable agreement in breakdown pressure, shut-in pressure, and the pressure decay trend during the shut-in period when compared with the observed data. Figure 5b shows the G-function plot (see Economides and Nolte (1989) for details) based on the modeled pressure curve, which indicates that fracture closure initiates when the BHP decreases to approximately 44.5 MPa, consistent with the minimum horizontal stress applied in the simulation.

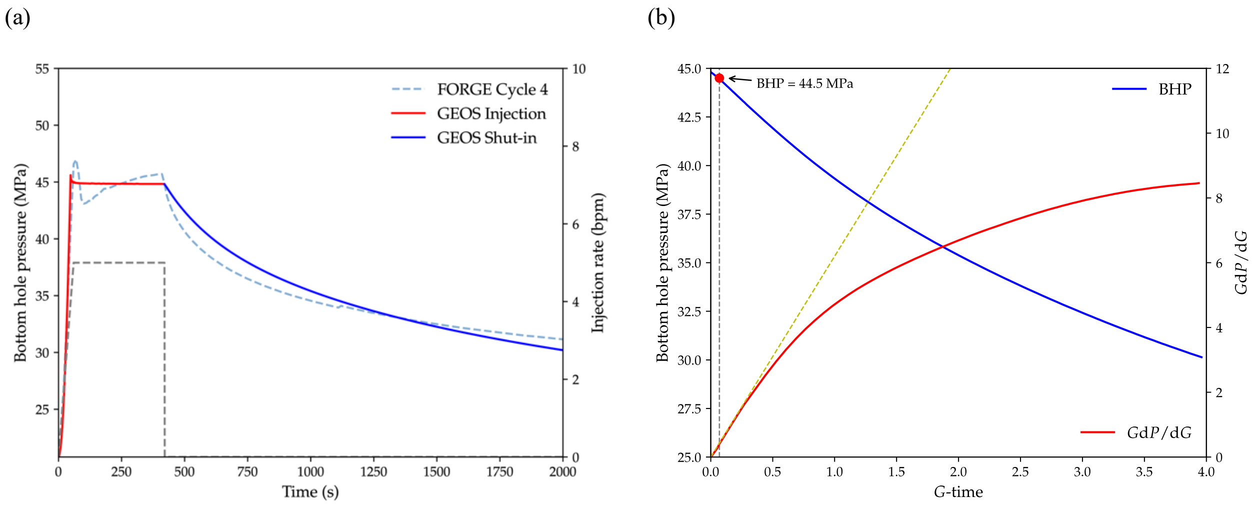

Figure 5: DFIT simulation of the *Cycle 4* test in Zone 2 of Well 58-32 using the exponential model (17): (a) comparison between the BHP curve obtained from GEOS and that from Utah FORGE; (b) *G*-function plot base on the modeled pressure.

All calibrated parameter values are consistent with those presented in the literature. The calibrated minimum horizontal stress from the numerical study (44.5 MPa) lies within the potential range (41.7–44.9 MPa) reported by Xing et al. (2020), in which various techniques have been applied to analyze the field data from the Zone 2 injection tests. To fit the observed BHP, our simulations require matrix permeability of 8×10^{-16} m^2, but is considerably higher than that of intact granite, which is typically around microdarcy (10^{-18} m^2). Note that in our numerical model, permeability should be treated as an effective permeability that accounts for the presence of preexisting natural fractures in rock matrix, which potentially provide additional hydraulic conductivity. Additionally, the calibrated fracture properties are consistent with those measured by relevant laboratory experiments where triaxial direct shear tests on FORGE core samples indicate that the fracture compressibility α is 0.25–0.35 MPa^{-1} (Kroll, et al., 2023). The initial aperture measured from the same experimental sample (~40 mm in height) is around 0.2 mm, which is much smaller than the calibrated values for the modeled fracture (~40 m in diameter). Nevertheless, we note that the initial aperture exhibits dependence on the fracture size, and according to the empirical relationship provided in Hatton et al. (1994) and Frash et al. (2019) for a tensile-driven fracture, we can estimate the upscaled ω_0 from experimental measurements, which gives $\omega_0 \approx 15.5$ mm. In this regard, use of $\omega_0 = 15$ mm in the model is justifiable.

4.3 Sensitivity to Fracture Properties

After calibration, we perform a parameter sensitivity study and present results in Figure 6 and Figure 7 to illustrate how the initial aperture ω_0 and the reference contact stress σ_{ref} individually affect the pressure curve in the shut-in stage. Figure 6a shows that a smaller ω_0 gives rise to an accelerated pressure decay. This phenomenon can be explained by the higher fracture stiffness resulting from a smaller ω_0 (see Eq. (20) and Figure 6b). Consequently, the contact stress increases more rapidly with a decreasing ω_h, which leads to a faster pressure dissipation. A similar analysis also applies to understand the effects of σ_{ref} as shown in Figure 7a: Figure 7b demonstrates that the fracture stiffness increases with σ_{ref}, thereby leading to an accelerated pressure drop as the fracture closes.

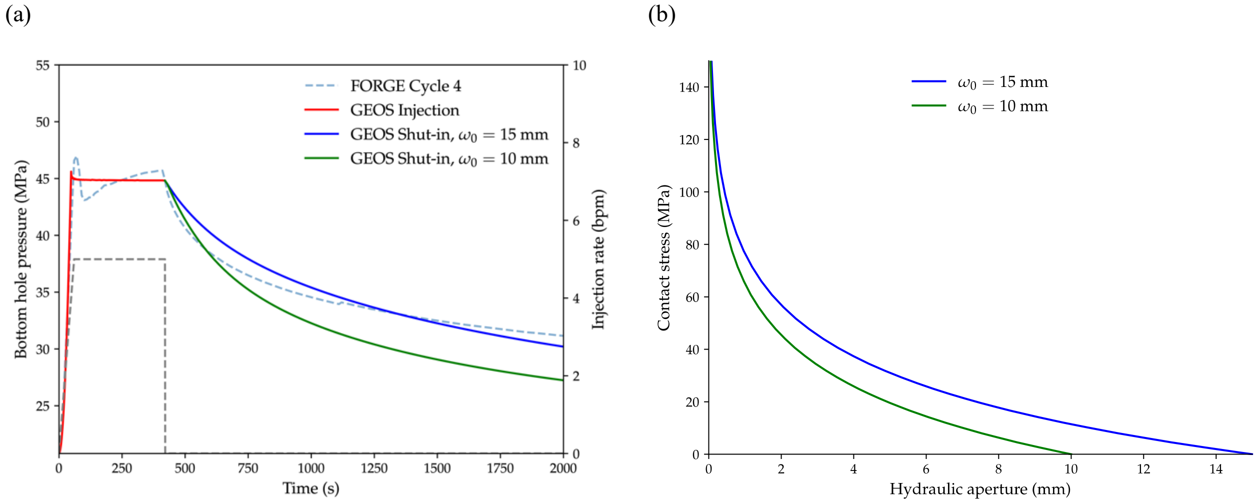

Figure 6: DFIT simulation of the *Cycle 4* test in Zone 2 of Well 58-32 with different initial apertures ω_0: (a) comparison of the BHP curves; (b) comparison of $\omega_h - \sigma_N$ relations.

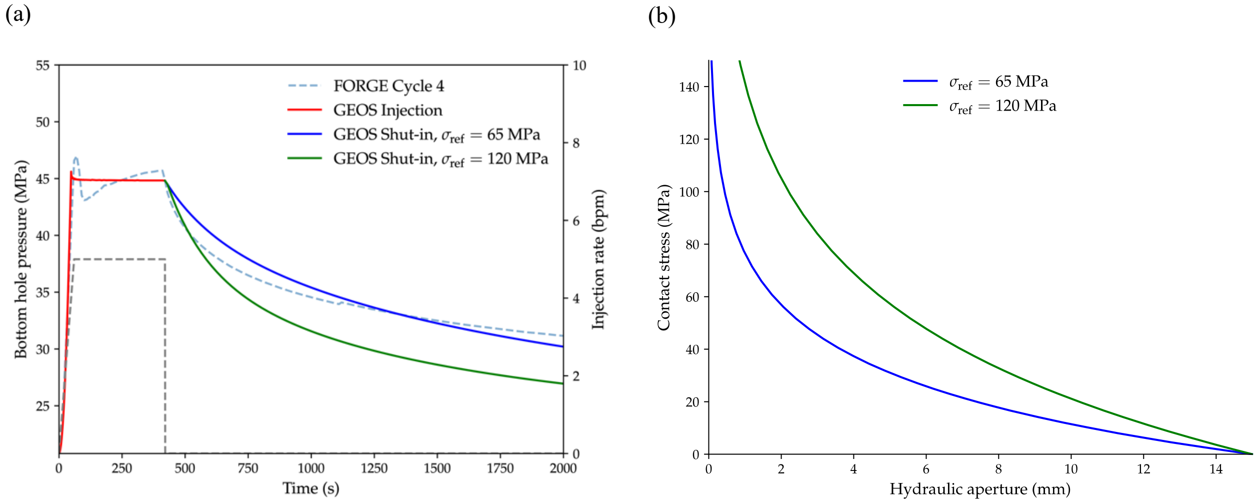

Figure 7: DFIT simulation of the *Cycle 4* test in Zone 2 of Well 58-32 with different reference contact stresses σ_{ref}: (a) comparison of the BHP curves; (b) comparison of $\omega_h - \sigma_N$ relations.

4.4 Sensitivity to the Hydraulic Aperture Model

Here, we explore the impact of the chosen hydraulic aperture model on simulation results. Specifically, we re-simulate the shut-in stage using the Barton–Bandis model (Eq. (16)), while all material parameters are held constant. Figure 8a shows a comparison of the results obtained using the two different aperture models for the same values of σ_N and ω_0. Noted that the pressure curve for the Barton–Bandis model after shut-in exhibits a nearly linear trend with a much slower decay rate, in contrast with the generally convex shape observed in both field data and simulation results for the exponential model. The discrepancy can be explained by analyzing the $\omega_h - \sigma_N$ relation in Figure 8b. When the fracture starts to close ($\omega_h \approx \omega_0$), the Barton–Bandis model demonstrates a slower increase in the contact stress due to a smaller fracture stiffness (see Eqs. (19) and (20)), which leads to a more gradual pressure reduction compared with the exponential model.

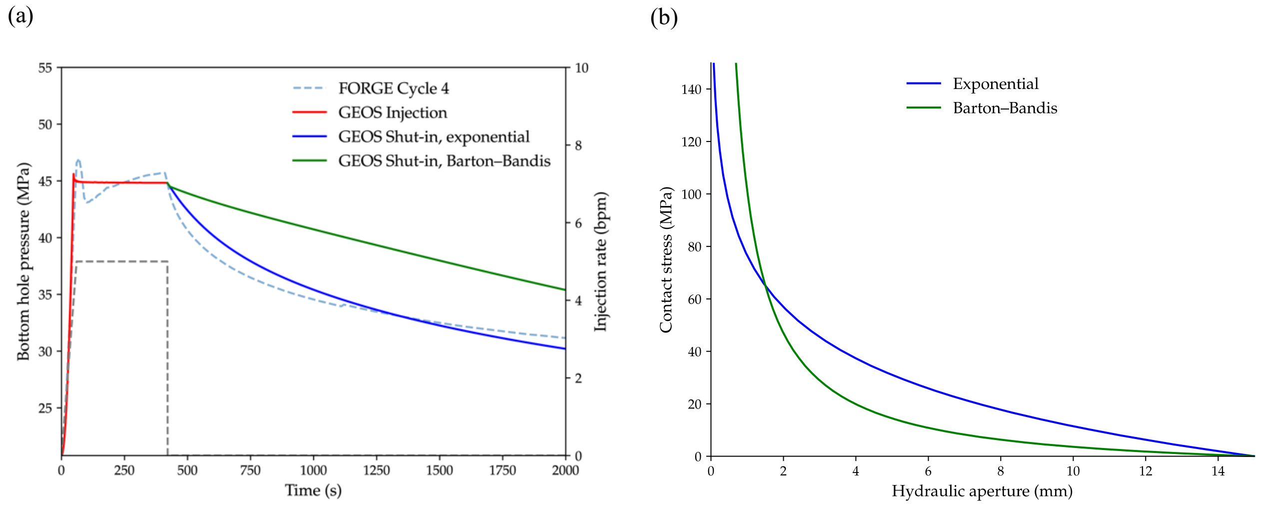

Figure 8: DFIT simulation of the *Cycle 4* test in Zone 2 of Well 58-32 with different hydraulic aperture models but same material parameters: (a) comparison of the BHP curves obtained from the Barton–Bandis model (16) and the exponential model (17); (b) comparison of $\omega_h - \sigma_\mathrm{N}$ relations for the Barton–Bandis model (16) and the exponential model (17).

Further refinement of the parameters of the Barton–Bandis model is required to achieve faster pressure decay observed in the field data. Figure 9 presents the simulated pressure curve obtained using the Barton–Bandis model with a higher reference contact stress ($\sigma_\mathrm{ref} = 200$ MPa), while other parameters remain unchanged. The resulting concave pressure curve more closely represents the field data, demonstrating that a well-calibrated Barton–Bandis model can also be used to reproduce the field data.

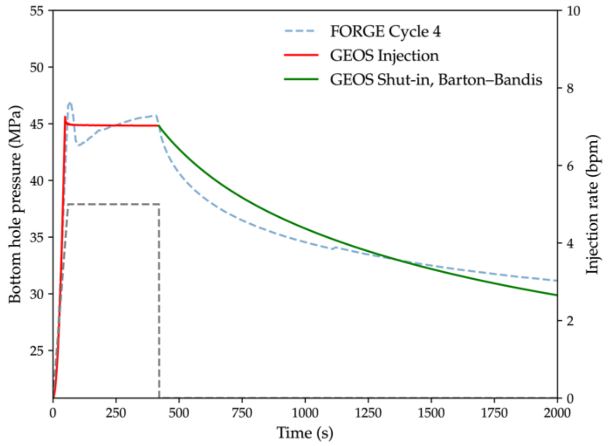

Figure 9: DFIT simulation of the *Cycle 4* test in Zone 2 of Well 58-32 using the Barton–Bandis model (16): comparison between the BHP curve obtained from GEOS and that from Utah FORGE.

4.5 Impact of Thermal Effects

All simulations conducted so far in this work are limited to isothermal conditions, where the thermal effects on fluid flow and mechanics are not considered. However, for EGS applications such as Utah FORGE, where thermal processes are of great importance and neglecting thermal effects when modeling and interpreting DFITs may lead to errors in the estimation of in situ stresses. Therefore, we extend the DFIT model presented in Section 2 to consider a non-isothermal condition by integrating the energy balance equation and thermal effects on the contact stresses into the formulation. For simplicity, we omit the detailed equations related to energy balance and thermo-hydraulic coupling, which can be found in Guo et al. (2016). To incorporate thermo-mechanical coupling, we include a thermal stress component when calculating the contact stress on the fracture by modifying Eq. (4) to

$$\boldsymbol{\sigma}\cdot\boldsymbol{n}_{\Gamma+} = -\boldsymbol{\sigma}\cdot\boldsymbol{n}_{\Gamma-} = -p_f\boldsymbol{n}_{\Gamma+} + K\alpha_s^T(T_m - T_0)\boldsymbol{n}_{\Gamma+} + \boldsymbol{t}_\Gamma \quad \text{on } \Gamma, \tag{22}$$

where K is the bulk modulus of the rock, α_s^T is the thermal expansion coefficient, T_m refers to the temperature of rock matrix neighboring the fracture, and T_0 is the initial temperature. Specific values of thermal properties adopted in the simulation are listed in Table 3.

Table 3: Thermal properties in the simulation

Volumetric heat capacity of the rock, C_s^T	1950 kJ/K/m^3
Thermal expansion coefficient of the rock, α_s^T	6×10^{-6} K^{-1}
Specific heat capacity of the fluid, C_f^T	4.2 kJ/K/kg
Thermal expansion coefficient of the fluid, α_f^T	0 K^{-1}
Thermal conductivity of rock matrix, k_m^T	3.81 W/m/K
Thermal conductivity of fracture, k_f^T	0.2 W/m/K
Thermal conductivity of rock-fracture interface, k_{fm}^T	200 W/m/K

Figure 10 compares the BHP for both isothermal and non-isothermal cases. Initially, both scenarios exhibit similar pressure trends at the onset of injection. However, as the injection progresses, the BHP in the non-isothermal case decreases and remains consistently lower than that in the isothermal case throughout the shut-in stage. This observed behavior under non-isothermal conditions can be attributed to the injection of cold water, which cools down the rock matrix surrounding the fracture and leads to a volumetric contraction. This contraction essentially exerts an additional force on the fracture walls, reducing the fluid pressure needed to sustain the in situ compressive stress. Notably, the pressure difference due to the non-isothermal condition is less than 1 MPa, because the DFIT activity involves limited injection volume. Also, we didn't model the circulation before the DFIT, which, if exists in Well 58-32, can pre-cool down the wellbore and significantly alter the initial stress field near the wellbore.

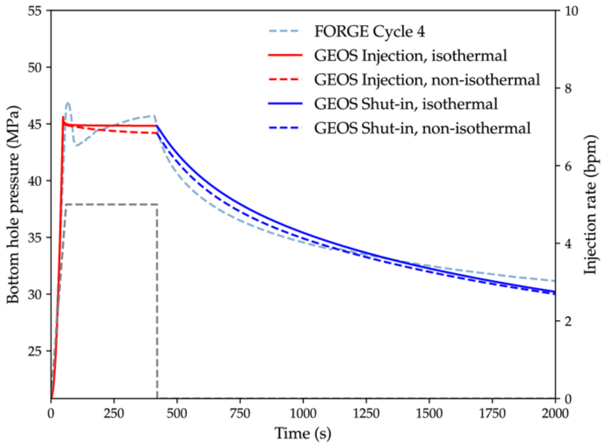

Figure 10: DFIT simulation of the *Cycle 4* test in Zone 2 of Well 58-32 under an isothermal or thermal condition.

5. CONCLUSIONS

To summarize, we have presented a computational tool to simulate hydraulic fracture propagation and employed it to model the *Cycle 4* injection test in Zone 2 of Well 58-32 at the Utah FORGE site. The following points merit additional emphasis:

- Both the Barton–Bandis model (16) and the exponential relation (17) can well match the field data from FORGE as long as appropriate parameters are adopted.
- The calibrated minimum horizontal stress from our numerical study is 44.5 MPa, which is consistent with the estimated value (41.7-44.9 MPa) suggested by Xing et al. (2020) based on the analyses of field data using various techniques. The resulting calibrated material parameters are similar to those found through experimental analysis on Utah FORGE core (Kroll, et al., 2023). The relatively high matrix permeability required by the model is an effective value which accounts for the existence of natural fractures. Also, the adopted value of initial aperture ω_0 is high compared to the experiment measure, but given the size dependence of ω_0, the value used in the simulation agrees well with upscaled ω_0.

- Thermal effects have an influence on the pressure evolution of the DFIT model due to additional tension on the fracture caused by the temperature drop on the fracture walls. However, these thermal effects are minimal, attributed to the limited injection volume and absence of pre-cooling before conducting the DFIT.

The current simulation results still show some discrepancies with the field data. For example, the numerical model produces a relatively flat pressure curve right after breakdown, while field data exhibits a gradual pressure increase. Potential causative mechanisms include (Xing, et al., 2021): (i) poroelastic effects and (ii) interactions between the hydraulic fracture and the network of natural fractures. Ongoing and future research applying this DFIT modeling tool is necessary to understand the impact of the two mechanisms on the pressure response, and will be combined with ongoing studies that model near-wellbore hydraulic fracturing (Fei, et al., 2023; Lu, et al., 2023).

ACKNOWLEDGEMENTS

This work relies on the GEOS simulation framework, and the authors wish to thank the GEOS development team for their contributions. The authors thank Utah FORGE for the financial support. This work was performed under the auspices of the U.S. Department of Energy by Lawrence Livermore National Laboratory under Contract DE-AC52-07NA27344.

REFERENCES

Barton, N., Bandis, S., and Bakhtar, K.: Strength, deformation and conductivity coupling of rock joints. *International Journal of Rock Mechanics and Mining Sciences & Geomechanics Abstracts, 22*(3), (1985), 121-140.

Batchelor, G. K.: *An introduction to fluid dynamics.* Cambridge University Press (1967).

Economides, M. J., and Nolte, K. G.: *Reservoir stimulation* (Vol. 2). Englewood Cliffs, NJ, USA: Prentice Hall (1989).

Fei, F., Lu, Y., Bunger, A. P., and Matteo, C.: Experimental and numerical study of hydraulic fracturing in enhanced geothermal systems (EGS). *48th Workshop on Geothermal Reservoir Engineering*. Stanford, CA (2023).

Frash, L. P., Carey, J. W., and Welch, N. J.: Scalable en echelon shear-fracture aperture-roughness mechanism: theory, validation, and implications. *Journal of Geophysical Research: Solid Earth, 124*, (2019), 957-977.

Guo, B., Fu, P., Hao, Y., Peters, C. A., and Carrigan, C. R.: Thermal drawdown-induced flow channeling in a single fracture in EGS. *Geothermics, 61*, (2016), 46-62.

Hatton, C. G., Main, I. G., and Main, P. G.: Non-universal scaling of fracture length and opening displacement. *Nature, 367*(6459), (1994), 160-162.

Kroll, K. A., Smith, M. M., Hao, Y., Davila, G., Fei, F., Wang, C., . . . Richards-Dinger, K.: *Coupled investigation of fracture permeability impact on reservoir stress and seismic slip behavior.* Lawrence Livermore National Laboratory. Livermore, CA, (2023).

Li, W., Frash, L. P., Welch, N. J., Carey, J. W., Meng, M., and Wigand, M.: Stress-dependent fracture permeability measurements and implications for shale gas production. *Fuel, 290*, (2021), 119984.

Lu, Y., Lu, G., Fei, F., Cusini, M., and Bunger, A. P.: Understanding in situ stress complexities in EGS reservoirs through true-triaxial block fracturing experiments on high temperature analogue Utah FORGE granites. *Geothermal Rising Conference.* Reno, NV, (2023).

McClure, M. W., Jung, H., Cramer, D. D., and Sharma, M. M.: The fracture-compliance method for picking closure pressure from diagnostic fracture-injection tests. *SPE Journal, 21*(4), (2016), 1321-1339.

Nordgren, R. P.: Propagation of a vertical hydraulic fracture. *Society of Petroleum Engineers Journal, 12*(04), (1972), 306-314.

Perkins, T., and Kern, L.: Widths of hydraulic fractures. *Journal of Petroleum Technology, 13*(09), (1961), 937-949.

Settgast, R. R., Fu, P., Walsh, S. D., White, J. A., Annavarapu, C., and Ryerson, F. J.: A fully coupled method for massively parallel simulation of hydraulically driven fractures in 3-dimensions. *International Journal for Numerical and Analytical Methods in Geomechanics, 41*(5), (2017), 627-653.

Willis-Richards, J., Watanabe, K., and Takahashi, H.: Progress toward a stochastic rock mechanics model of engineered geothermal systems. *Journal of Geophysical Research: Solid Earth, 101*(B8), (1996), 17481–17496.

Wu, H., Settgast, R. R., Fu, P., and Morris, J. P.: An enhanced virtual crack closure technique for stress intensity factor calculation along arbitrary crack fronts and the application in hydraulic fracturing simulation. *Rock Mechanics and Rock Engineering, 54*(6), (2021), 2943-2957.

Xing, P., Damjanac, B., Radakovic-Guzina, Z., Finnila, A., Podgorney, R., Moore, J., and McLennan, J.: Numerical simulation of injection tests at Utah FORGE site. *46th Workshop on Geothermal Reservoir Engineering.* Stanford, CA, (2021).

Xing, P., McLennan, J., and Moore, J.: In-situ stress measurements at the Utah frontier observatory for research in geothermal energy (FORGE) site. *Energies, 13*(21), (2020), 5842.